SAR Imaging and Multiresolution Analysis

Gregory Beylkin[1], John D. Gorman[2], Sylvia Li-Fliss[2] and Mark A. Ricoy[2]

[1]Program in Applied Mathematics University of Colorado-Boulder 80309

[2]Environmental Research Institute of Michigan Box 134001, Ann Arbor, Michigan 48113-4001

ABSTRACT

Many synthetic aperture radar (SAR) image formation algorithms require the computation of a multidimensional Fourier transform of irregularly-sampled or unequally-spaced data samples. We apply a recently developed algorithm, the *unequally-spaced FFT* (USFFT),[2] to SAR image formation and compare its accuracy and complexity to a conventional algorithm. We find that the USFFT algorithm allows comparable accuracy to traditional approaches at a slightly reduced computational cost. We briefly discuss extensions of the USFFT algorithm to multiresolution SAR imaging.

Keywords—*Synthetic Aperture Radar, Image Reconstruction, Multiresolution Analysis.*

1 Introduction

We investigate the application of a new tool, the *unequally-spaced FFT* (USFFT),[2] for SAR image formation. To simplify the development we will focus on polar-format processing of spotlight-mode SAR data for a SAR operating near broadside.[11] Nonetheless, the concepts we present here can be extended to work under a variety of SAR imaging modalities, including certain stripmap SAR algorithms[3] and range-migration algorithms.[5]

In polar-format SAR, the radar data is collected on a polar grid in the Fourier domain. Digital polar-format SAR processors typically consist of three stages, polar-to-rectangular interpolation, inverse FFT, and amplitude correction. Sinc interpolation is commonly used for the polar-to-rectangular interpolation. However, the sinc function has infinite extent and decays rather slowly (i.e., as $1/x$). A practical approach is to use a truncated sinc or a weighted and truncated sinc. Here, accuracy is traded for computational speed by reducing the number of samples used in the interpolator. When the unequally-spaced data lie on a nearly-rectangular grid, further speed is gained by approximating the nonseparable interpolation kernel by a separable one. Many polar format SAR processors perform 1D interpolation along range followed by 1D azimuth interpolation.[1,7]

In its most basic application, the USFFT algorithm for polar-format SAR has essentially the same sequence of steps as a conventional polar-format algorithm. Specifically, the USFFT algorithm consists of three steps[2]: multiresolution spline projection (interpolation) onto a rectangular grid, inverse FFT, and amplitude correction. We show in Section 2 that the USFFT spline bases provide comparable or better accuracy than conventional interpolation filters of equivalent length. A key attribute of the spline projection operation is that there are simple analytical formulas for the interpolation filters and their accuracy. This is in contrast to previous approaches

 0-8194-1840-4/95/$6.00

such as the Parks-McClellan digital filter which is obtained by nonlinear optimization of a discrete function. Reference 2 derives an explicit error bound in terms of USFFT algorithm parameters. This bound allows the design of SAR reconstruction algorithms having a prespecified accuracy.

More importantly, the USFFT has a natural adaptation to multiresolution processing. In Section 3, we briefly discuss multiresolution extensions of the USFFT-based polar-format SAR algorithm. These multiresolution algorithms exploit analogies between subband filtering and subpatch processing, multiresolution analysis and subaperture processing. Potential applications of a multiresolution image formation algorithm are SAR bandwidth compression, image previewing, ATR, fast scene screening. We briefly discuss applications of multiresolution SAR processing in operational systems and provide example multiresolution reconstructions.

1.1 Image Model

We will assume that the radar system parameters satisfy conditions required for polar-format processing.[1,11] Let $\sigma(x,y)$ denote the complex reflectivity function of the scene being imaged, where x is the azimuth or along-track coordinate and y is the slant-range coordinate. Let $B \times B$ be an area in the (x,y) plane covered by the radar footprint. We assume the radar uses a linear FM chirp waveform. After deramping (demodulating) and sampling the received echoes, the SAR data s approximates the Fourier transform of σ,

$$s(\theta_k, r_l) = C \int_B \int_B \sigma(x,y) \exp\left\{i2\pi(x \cdot r_l \sin\theta_k + y \cdot r_l \cos\theta_k)\right\} dxdy, \tag{1}$$

sampled on a *polar* grid at locations given by:

$$\theta_k = \theta_0 + k \cdot \Delta\theta = \theta_0 + k \cdot PRF \quad k = 1, \ldots, K \tag{2}$$

$$r_l = r_0 + l \cdot \Delta r = \frac{2f_0}{c} + l \cdot \kappa_r \frac{c}{2SW\gamma}, \quad l = 1, \ldots, L. \tag{3}$$

We assume a total of K pulses are collected, with each pulse containing L samples.

In (1), C is a complex-valued term that includes quadratic phase terms (including residual video phase[11]) which we ignore in this paper. Important system parameters are:

$$\begin{aligned} \theta_0 &= \text{initial radar look angle (degrees)} \\ PRF &= \text{pulse repetition frequency (Hz)} \\ f_0 &= \text{starting frequency of chirp (Hz)} \\ c &= \text{propagation constant (m/s)} \\ SW &= \text{range swath width (m)} \\ \gamma &= \text{chirp rate (Hz/s)} \\ \kappa_r &= \text{range oversampling factor.} \end{aligned}$$

The bandwidth of each deramped pulse depends on the chirp rate γ and the radar swath width SW, and is nominally $2SW\gamma/c$. However, one typically samples at a rate slightly higher than Nyquist to avoid aliasing effects. A typical value for the oversampling factor is $\kappa_r = 1.2$.

Typical PRF constraints are[1,6]:

$$\frac{c}{2SW} \geq PRF \geq \frac{4v}{D}, \tag{4}$$

where

$$\begin{aligned} v &= \text{platform velocity (m/s)} \\ D &= \text{antenna diameter (m).} \end{aligned}$$

The PRF lower bound is chosen to avoid aliasing the Doppler (azimuth) frequencies, while the upper bound is required to avoid *eclipsing* problems in which the radar echoes overlap in time.

1.2 Polar-Format SAR Image Formation

Construction of a linear image reconstruction algorithm essentially requires that we determine the weights $\omega(\theta_k, r_l)$ that best approximate the inverse Fourier integral,

$$\sigma(x,y) = \int_{\Theta}\int_{R} s(\theta,r)\exp\{-i2\pi(xr\sin\theta + yr\cos\theta)\}rdrd\theta \simeq \sum_{k,l} s(\theta_k, r_l)\omega(\theta_k, r_l), \tag{5}$$

where $\Theta = [\theta_0, \theta_0 + K\Delta\theta)$ and $R = [r_0, r_0 + L\Delta r)$, and $\Theta \times R$ is the synthetic aperture. The more efficient polar-format SAR schemes exploit FFT techniques by resampling from polar coordinates onto a cartesian grid.

The finite radar beamwidth implies that the observed reflectivity function $\sigma(x,y)$ in Equation (1) goes to zero outside of the beam footprint $B \times B$. Consequently, the deramped phase history data $s(\theta_k, r_l)$ is *bandlimited* and conventional interpolation techniques can be used to resample s onto a rectangular grid. Let $s(\xi_{k'}, \eta_{l'})$ denote the resampled version of $s(\theta_k, r_l)$. Digital polar-format SAR processing consists of three steps[1]:

1. **Resample onto rectangular grid.** Here, we resample from a $K \times L$ polar grid onto a $K' \times L'$ rectangular grid:

$$s(\xi_{k'}, \eta_{l'}) = \sum_{k,l} s(\theta_k, r_l) h\left(\xi_{k'} - r_l\sin\theta_k, \eta_{l'} - r_l\cos\theta_k\right). \tag{6}$$

   Function h is an interpolation filter. The (ξ, η) sample spacing is chosen to be *coarser* than the original polar grid (i.e., the interpolator does not "upsample" the phase history data). Equivalently,

$$\begin{aligned} \xi_{k'} &= \xi_0 + k'\Delta\xi, \quad \Delta\xi \geq \Delta r, \quad k' = 1, \ldots K' \\ \eta_{l'} &= \eta_{l'} + l'\Delta\eta, \quad \Delta\eta \geq r_K\Delta\theta, \quad l' = 1, \ldots, L'. \end{aligned}$$

   The output array size, $K' \times L'$, satisfies $K' \leq K$ and $L' \leq L$, and is chosen based on the desired scene size. The maximum scene size is roughly equal to the beam footprint $B \times B$ and is achieved by choosing K' and L' to be as large as possible without aliasing the interpolated data.

2. **Zero Pad and Inverse FFT.** We use the FFT to invert Equation (1) and reconstruct a discretized version of $\sigma(x,y)$. It is common to *zero pad* the interpolated phase history data (6) by embedding it into a larger array of size $M \times N$ (where $M > K', N > L'$) prior to inverse FFT,

$$F(x_m, y_n) = \sum_{k',l'} w(\xi_{k'}, \eta_{l'}) s(\xi_{k'}, p\eta_{l'}) \exp\left\{-i2\pi\left(\frac{mk'}{M} + \frac{nl'}{N}\right)\right\}. \tag{7}$$

   Zero padding the phase history data yields an upsampled image. One typical upsampling factor is $M = 3K'/2, N = 3L'/2$, which gives a sampling rate of 1.5 pixels per resolution cell. An optional weighting function w is typically applied in (7) to suppress sidelobes.[10]

3. **Amplitude Correction and Image Trim.** Finally, an amplitude correction is typically applied after the inverse FFT to compensate for the non-uniform response in the passband of the interpolation filter h in the image domain,

$$\sigma(x_m, y_n) = \frac{F(x_m, y_n)}{A(x_m, y_n)}. \tag{8}$$

After amplitude correction, the image is "trimmed" to remove image pixels at the edge of the scene that fall within the transition band of the interpolator. A total of $M' \times N'$ pixels are extracted.

We compare the two polar-format SAR image formation algorithms, a conventional algorithm that uses separable sinc interpolation and a USFFT-based version. In our comparison in Section 2, we refer to the conventional algorithm as the "baseline." Both reconstruction algorithms implement Equations (6), (7) and (8). The main differences lie in the interpolation and amplitude correction steps.

Baseline Algorithm (separable sinc interpolation):

We use separable sinc interpolation in the baseline algorithm. Separable interpolation can be used when the original polar grid is nearly rectangular. One approach is to perform 1D interpolation along range followed by a 1D interpolation along azimuth.[1,7] Here, h to is a weighted, truncated sinc function and (6) is rewritten as a *separable* summation:

$$s(\xi_{k'}, \eta_{l'}) = \sum_k \left\{ \sum_l s(\theta_k, r_l) \text{sinc}\left(\frac{\eta_{l'} - r_l \cos\theta_k}{B} \right) \right\} \text{sinc}\left(\frac{\xi_{k'} - \eta_{l'} \sin\theta_k}{B} \right). \quad (9)$$

There can be a fair degree of oscillation (ripple) in the passband of the interpolator, particularly if the sinc function is truncated to a small number of samples. The amplitude correction A in (8) is commonly applied in the image domain to remove these oscillations which would otherwise show up as image artifacts.

USFFT-based Algorithm (multiresolution-spline projection):

The USFFT algorithm replaces sinc interpolation with projection onto a multiresolution spline basis. Here, (6) is replaced by:

$$s(\xi_{k'}, \eta_{l'}) = \sum_{k,l} s(\theta_k, r_l) \beta_{jk'}^{(m)}(r_l \sin\theta_k) \beta_{jl'}^{(m)}(r_l \cos\theta_k), \quad (10)$$

where, $\beta_{jk}^{(m)}(x) = 2^{-j}\beta^{(m)}(2^{-j}x - k)$ is the mth-order central B-spline,[9] where the *scale* j is chosen so that $2^{-j} = K'$, and K' is the resampled grid size. The amplitude correction A in (8) is chosen so that the resulting basis is the orthonormal Battle-Lemarié basis.[2]

Finally, we note that a separable version of the USFFT algorithm can be implemented for computing the Fourier transform of points sampled on a nearly uniform sampling grid. We will report on a separable USFFT SAR image formation algorithm in a separate paper.

2 Comparison

In order to compare the USFFT with existing algorithms, let us first adopt a traditional point of view and consider the USFFT projection step as a standard interpolation operation. Although the steps of the USFFT algorithm are the same as in previous approaches, there is a difference in the way one may view the design of the interpolation filters. In the traditional approach, an attempt is made to approximate an ideal (rectangular) filter as close as possible, which implies an oscillatory behavior in the Fourier domain. The amplitude correction step (8) is typically applied to compensate for oscillatory behavior within the filter passband.

In the USFFT approach, the ideal filter is not approximated in a close manner. Namely, $\hat{\beta}^{(m)}(\xi)$, the Fourier

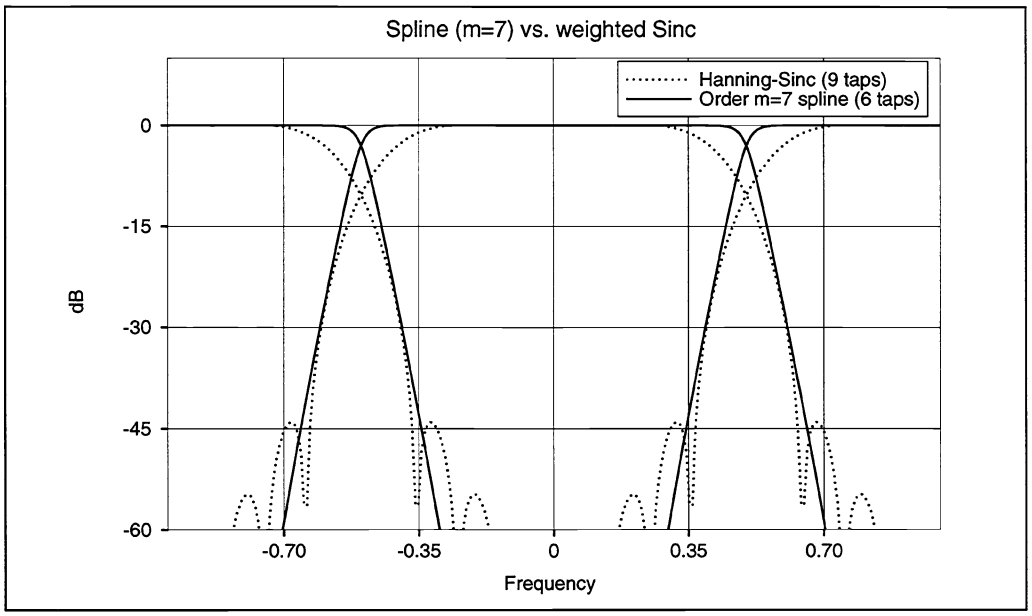

Figure 1: Order 7 Spline (6 taps) versus Hanning-weighted sinc (9 taps)

transform of the B-spline, cannot be considered as an approximation of the ideal filter. The correction in the Fourier domain is done not for the purpose of removing residual oscillations, but to finish the construction of an approximation to the ideal filter. The resulting filters are the so-called Battle-Lemaré scaling functions.[2] The cumulative result is a family of filters with excellent spectral characteristics. We present three examples where we compare these Battle-Lemarié filters with two commonly-used SAR interpolation filters, a 9-point Hanning-weighted sinc and a 10-point filter designed via the Remez-exchange algorithm due to Parks and McClellan.

Interpolation is inherently a lowpass filtering operation and the final reconstructed image $\sigma(x, y)$ will be weighted by the 2D passband characteristic of the interpolator. Portions of the scene that appear at the edge of the image can be heavily attenuated or may contain aliasing artifacts due to inadequate sampling of the phase history signal. These edge artifacts are usually trimmed from the imagery. The size of the final $M' \times N'$ image depends on the effective spectral characteristics of the interpolator and the desired image accuracy. The size of the region that needs to be trimmed may be implied from the spectral characteristics of the of the interpolation filter.

Figure 1 shows the effective spectral characteristics of the Hanning-weighted sinc interpolator and the order $m = 7$ spline projection (after amplitude correction). The first sidelobe of the Hanning-weighted sinc has a level of approximately -45dB. Also shown are plots of the (periodic) spectra centered at frequencies -1 and 1. Assuming that the desired image accuracy is -45dB, the usable portion of the spectrum is the range $[-0.35, 0.35]$, or 70% of the nominal filter bandwidth. The order $m = 7$ spline has a similar characteristic: aliasing errors fall below -45dB over the range $[-0.35, , 0.35]$. We implement the order $m = 7$ spline using a six-tap filter using the approach explained below. An implication of the aliasing artifact is that only 49% of the image pixels (i.e., 0.7×0.7) are retained in final image. Equivalently, we require that the phase history be oversampled by a factor of 1.3 in both the range and azimuth directions (i.e., we need to use a $1.3M' \times 1.3N'$ FFT in order to guarantee a level of -45dB accuracy over a $N' \times M'$ final image array).

Figure 2 shows the effective spectral characteristics of a 10-point Parks-McClellan filter as compared to an order $m = 13$ spline projection filter. The Parks-McClellan filter shown in Figure 2 was designed to have a

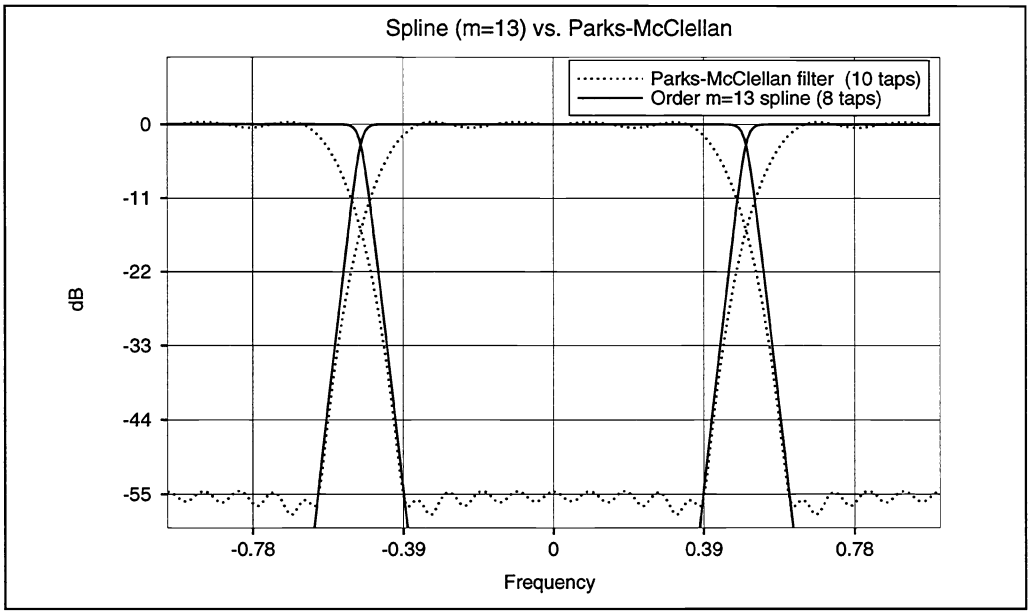

Figure 2: Order 13 Spline (8 taps) versus Parks-McClellan (10 taps)

Filter	*# Coefs.*	*# Coefs.* $> \epsilon$	ϵ *(dB)*	*% usable 1D spectrum*
Spline, $m = 7$	8	6	$\approx$ -45	70%
9 pt Hanning-Sinc	∞	9	$\approx$ -44	70%
Spline, $m = 13$	14	8	$\approx$ -67	78%
10 pt Parks-McClellan	10	10	$\approx$ -55	78%
Spline, $m = 19$	20	10	$\approx$ -73	82%

Table 1: Spline Approximation

stop-band rejection level of approximately -55dB. Here, -55dB accuracy is attained over the region $[-0.39, 0.39]$, and we require an oversampling factor of 1.22 in both the range and azimuth.

We can take advantage of the finite accuracy requirement and replace the spline projection (10) with an approximation. Spline coefficients that fall below the required accuracy limit don't need to be applied. This approximation results in a reduction of the number of filter taps require to implement the spline projection. Table 1 summarizes number of taps we need to keep in our examples to achieve the same level of accuracy as in the conventional interpolation filters. As an example, in Figure 2, for an $m = 19$ spline projection one needs only apply 10 coefficients to achieve an accuracy of greater than approximately -73 dB.

Figure 2 shows the effective spectral characteristic of an order $m = 19$ spline projection compared to the 10-point Parks-McClellan filter. A 10-tap approximation to the order $m = 19$ spline has the same level of accuracy as the Parks-McClellan filter, i.e., -55dB. Moreover, this accuracy is maintained over a larger interval, $[-0.42, 0.42]$. After image trimming, the $m = 19$ USFFT algorithm would keep 67% of the image pixels, as compared to the Parks-McClellan filter which would keep only 61% of the image pixels. Equivalently, the range and azimuth oversampling factors could be reduced from 1.22 to 1.18, if the USFFT algorithm is used.

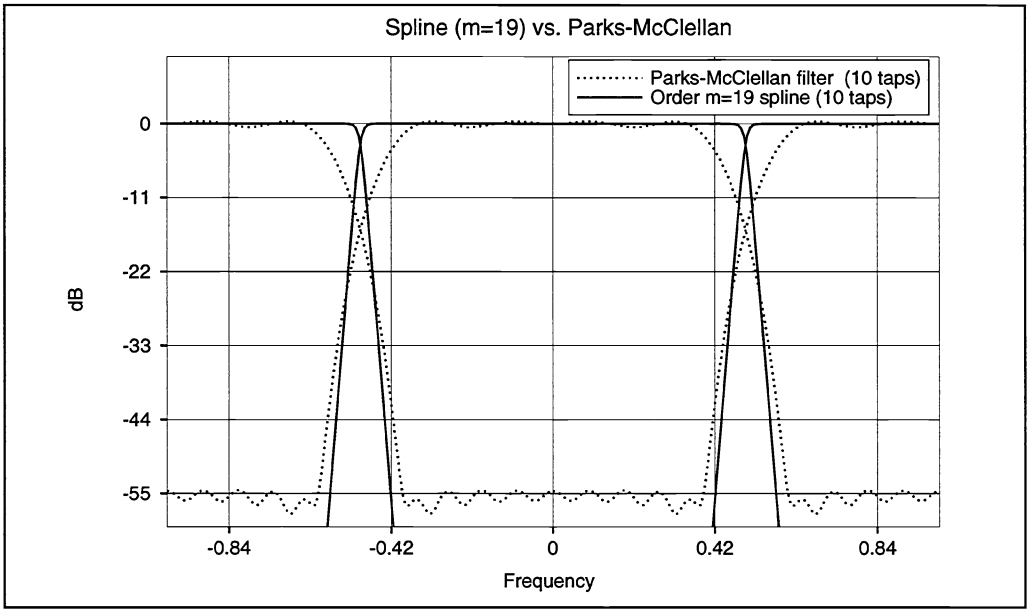

Figure 3: Order 19 Spline (10 taps) versus Parks-McClellan (10 taps)

3 Multiresolution Image Formation

For large scene sizes, the main computational burden in polar-format processing is the FFT. Memory limitations in early digital computers motivated digital SAR processor researchers to develop alternate reconstruction algorithms replace the Fourier integral in (5) with several smaller Fourier integrals that were easily accomplished via small FFTs. Many of these algorithms can be written in the form

$$\sigma(x,y) = \sum_{j=1}^{J} \int_{\Theta}\int_{R} P_j s(\theta,r) \exp\{-i2\pi(xr\sin\theta + yr\cos\theta)\} r dr d\theta. \tag{11}$$

Two examples are *subaperture processing*[1,8] and *subpatch processing.*[1]

We briefly describe the subaperture and subpatch processing algorithms and then show how the multiresolution spline projection (10) can be modified to achieve a decomposition of the form (11).

Subaperture Processing:

The basic idea behind subaperture processing is to subdivide the collection aperture $\Theta \times R$ into several smaller, possibly overlapping apertures $\{A_j, j = 1, \ldots, J\}$, so that $\Theta \times R \subset \cup_{j=1}^{J} A_j$. The inverse equation (5) is then replaced by

$$\sigma(x,y) = \sum_{j=1}^{J} \iint_{A_j} w(\theta,r) s(\theta,r) \exp\{-i2\pi(xr\sin\theta + yr\cos\theta)\} r dr d\theta, \tag{12}$$

where $w(\theta,r)$ is a weighting function. In (12), a large $M \times N$ FFT operation is replaced by J smaller ones.

Subpatch Processing:

Subpatch processing is the Fourier dual of subaperture processing. In subpatch processing, we perform a spec-

tral decomposition the phase history signal $s(\theta, r)$ by sending it through a bank of bandpass filters, $\{h_j(\theta, r), j = 1, \ldots, J\}$. These filtered versions of the phase history are called *subbands*. Assume that $\{h_j, j = 1 \ldots, J\}$ is a complete (possibly overcomplete) basis for $L^2(\Theta \times R)$, the set of all finite energy functions over $\Theta \times R$. Define the projection P_j to be the operation of filtering s with h_j,

$$P_j s(\theta, r) = \int_{\Theta}\int_{R} s(\theta', r') h_j(\theta - \theta', r - r') r dr d\theta. \tag{13}$$

Then the inverse Fourier transform of $P_j s(\theta, r)$ is equal to a *windowed* version of $\sigma(x, y)$:

$$H_j(x, y)\sigma(x, y) = \int_{\Theta}\int_{R} P_j s(\theta, r) \exp\{-i2\pi(xr\sin\theta + yr\cos\theta)\} r dr d\theta. \tag{14}$$

Here, H_j is the Fourier transform of filter h_j.

The USFFT is well suited for subpatch processing since the projection operation produces coefficients of the image on a subspace of a multiresolution analysis associated with splines. The basis can be chosen to be that of the B-splines, dual B-splines, or Battle-Lemarié. We thus can show that subpatch processing amounts to the wavelet-packet or full subband decomposition of the phase history data. Details and applications of this decomposition will be described at a later date.

4 Summary

We applied a recently developed tool, the *unequally-spaced FFT* (USFFT)[2] to polar-format SAR image formation and compared its performance to a contentional digital polar-format SAR processor. An analytic error bound developed in Reference 2 allows one to choose USFFT parameters to achieve a prespecified accuracy. In our comparisons we found that the USFFT algorithm yielded comparable or better accuracy for a given interpolation filter length.

5 Acknowledgement

This research was funded by ARPA/STO under the ARPA University ATD/R Initiative and the ARPA University/Industry ATD/R Initiative, contracts F33615-90C-1451 and F49620-93-1-0474.

6 REFERENCES

[1] D. A. Ausherman, A. Kozma, J. L. Walker, H. M. Jones, and E. C. Poggio, "Developments in Radar Imaging," IEEE Trans. Aero and Elec. Sys., vol. AES-20, no. 4, July 1984.

[2] G. Beylkin, "On the Fast Fourier Transform of Functions with Singularities," submitted to *Applied & Computational Harmonic Analysis,*, 1995 (also available as a preprint via anonymous FFT at `amath-ftp.colorado.edu`).

[3] Curlander and McDonough, "Synthetic Aperture Radar,"

[4] C. deBoor, *A Practical Guide to Splines,* Springer Verlag, New York, 1979.

[5] F. Rocca, C. Cafforio and C. Pratti, "Synthetic Aperture Radar: A New Application for Wave Equation Techniques," *Geophys. Prosp.,* v. 37, n. 7, 1989.

[6] A. Kozma, R. Shuchman, J. L Walker, D. Ausherman, C. Wackerman, R. Onstott, R. Heimiller, R. Mitchel, J. D. Gorman, *Synthetic Aperture Radar Technology and Applications,* Course Notes, University of Michigan, 1994.

[7] D. G. Munson, J. D. O'Brien and W. K. Jenkins"A Tomographic Formulation of Spotlight-Mode Synthetic Aperture Radar ," *Proc. IEEE*, v. 71, no. 8, August 1993.

[8] R. Perry, R. C. DiPietro, B. L. Johnson, A. Kozma and J. J. Vaccaro, "Planar Subarray Processing for SAR Imaging," to be presented at the 1995, IEEE National Radar Conference, Washington, D. C., May 1995.

[9] I.J. Schoenberg. *Cardinal Spline Interpolation.* SIAM, 1973. CBMS-NSF Series in Applied Math. #12.

[10] "Table of Taylor weights for radar,"

[11] J. L. Walker, "Range-Doppler Imaging of Rotating Objects," *IEEE Trans. Aero. and Elec. Sys.,* v. AES-16, January 1980.